

Electric-Switchable Chiral Magnons in \mathcal{PT} -Symmetric Antiferromagnets

Jinyang Ni,^{1,*} Congzhe Yan,^{2,3,*} Peiyuan Cui,² Zhijun Jiang,^{1,†} Yuanjun Jin,^{4,‡} and Guoqing Chang^{2,§}

¹*Ministry of Education Key Laboratory for Nonequilibrium Synthesis and Modulation of Condensed Matter, Shaanxi Province Key Laboratory of Advanced Functional Materials and Mesoscopic Physics, School of Physics, Xi'an Jiaotong University, Xi'an 710049, China*

²*Division of Physics and Applied Physics, School of Physics and Mathematical Sciences, Nanyang Technological University, Singapore 637371, Singapore*

³*Department of Physics, University of Science and Technology of China, Hefei, Anhui, 230026, China*

⁴*Guangdong Basic Research Center of Excellence for Structure and Fundamental Interactions of Matter, Guangdong Provincial Key Laboratory of Quantum Engineering and Quantum Materials, School of Physics, South China Normal University, Guangzhou 510006, China*

(Dated: January 23, 2026)

The magnons in antiferromagnetic insulators (AFIs) exhibit dual chirality, each carrying opposite spin angular momentum. However, in AFIs that are protected by \mathcal{PT} symmetry, the magnon bands remain degenerate. In this work, we introduce a new class of \mathcal{PT} -preserving AFIs in which the giant chiral splitting of magnons can be induced and reversibly controlled by an external electric field. Unlike ordinary cases, such AFIs host a hidden dipole coupled to the antiferromagnetic order, which allows an external electric field to break the magnon sublattice symmetry and thereby largely lift the band degeneracy. Through group theory analysis, we identify the possible magnetic layer groups that support electric-field-induced magnon band splitting. Promisingly, by density-functional-theory and spin wave calculations, the magnon band splitting of Cr_2CBr_2 reaches up to 27 meV induced by an electric field of 0.2 V/Å, equivalent to the 230 T under a uniform magnetic field. In addition, since chiral splitting is directly coupled to the electric field, the corresponding magnon-mediated spin current can be switched by the electric field. Our Letter opens a door for developing electric-field-controlled spintronics based on the magnons.

Introduction. The study of magnetic excitations provides critical insights into fundamental properties of bosons, as well as the applications of magnetic materials [1–10]. Being the elemental spin excitations in ordered magnets, magnons can carry spin angular momentum [1, 2, 11–14], which can be harnessed for information encoding and processing [15–19]. Unlike electrons, magnons can propagate over long distances in insulators without Joule heating, thereby overcoming the fundamental limitations of modern electronics [1, 2, 4, 6, 7, 20]. Moreover, magnons, with wavelengths several orders of magnitude shorter than photons at the same frequency, pave the way for wave-based information devices at the nanometer scale [1, 2, 21].

Conventional ordered magnets can be classified into ferromagnets and antiferromagnets, with the properties of their respective elementary spin excitations being fundamentally distinct. In ferromagnets, magnons (ferromagnons) are polarized with a right-handed chirality [2]. In contrast, antiferromagnets host magnons (antiferromagnons) that naturally possess both left-handed and right-handed chiralities [4, 22–24]. At zero wave vector, the quadratic dispersion relation for ferromagnons, $\epsilon(\mathbf{k}) \propto \mathbf{k}^2$, restricting their propagation frequency to the gigahertz (GHz) range, while for antiferromagnons follow a linear dispersion relation, $\epsilon(\mathbf{k}) \propto \mathbf{k}$, typically allowing them to operate in the terahertz (Thz) range [24, 25]. However, two chiral modes are degenerate under the \mathcal{PT} symmetry in antiferromagnons, which prevents the generation of spin current or net spin accumulation, limiting

their potential applications. One way to overcoming this limitation is to apply a strong magnetic field, though the resulting energy band splitting is quite small [22, 24, 26]. Furthermore, the bond exchange by strong spin-orbit coupling (SOC) can split the magnon bands, but intense SOC leads to the non-conservation of spin angular momentum, which in turn increases dissipation effects [27–30].

Recent studies have established that in altermagnets, a novel class of collinear antiferromagnets [31–37], the magnon modes exhibit nonrelativistic band splitting (or altermagnons) [8, 38–43]. This splitting arises from the breaking of translational and inversion symmetry that link two spin-compensated sublattices, enabling the alternating chiral splitting. Meanwhile, the unique symmetry significantly restricts the variety of altermagnons, and to date, only a few altermagnons have been confirmed [40, 41, 44]. In addition, the symmetry constraint renders external field manipulation. Therefore, realizing magnons with robust splitting and external field tunability remains a major challenge in the field of spintronics.

In this work, we identify a new class of \mathcal{PT} -preserving AFIs, where magnons exhibit giant chiral splitting solely induced by an electric field. Such AFIs feature hidden dipole coupled to the antiferromagnetic order, allowing the electric field breaks the sublattices of magnons. Notably, this results in significant changes in the isotropic spin exchange between opposite-spin sublattices in the presence of a finite electric field, resulting in the magnon bands splitting. By enumerating the possible magnetic

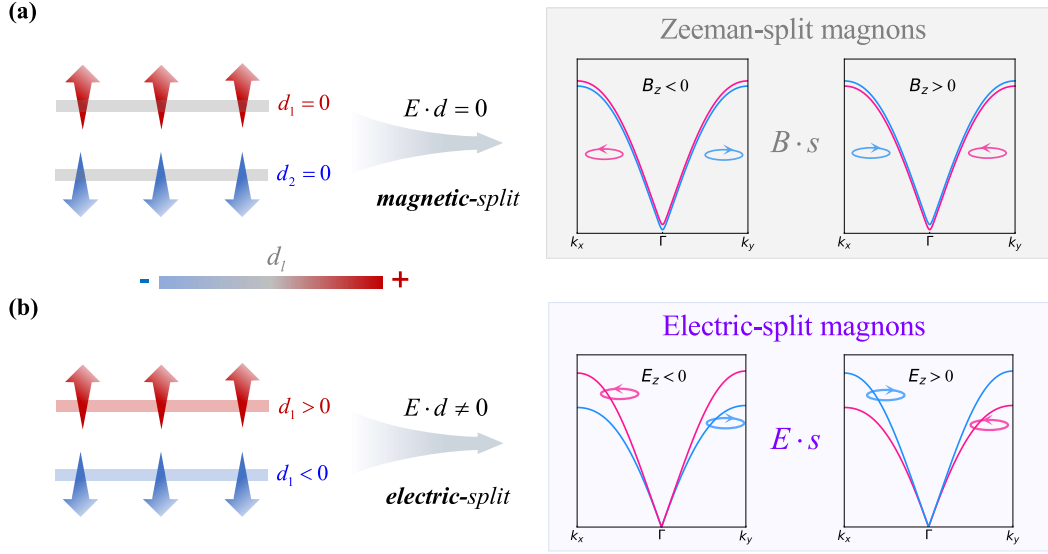


FIG. 1. The illustration of the magnons antiferromagnet with \mathcal{PT} symmetry. (a) The degenerate magnons when the local dipole (d_l) is absent, where only the Zeeman field can split the bands. (b) The degenerate magnons undergo electric-field-induced splitting in the presence of local polarization. Here, the red circle and blue circle represent the right-hand and left-hand chirality of magnons.

TABLE 1. Magnetic layer groups with high symmetry enabling electric field-driven magnon band splitting in antiferromagnets. The complete classification are listed in the Sec. IV of SM [45].

Point group	Magnetic layer group	Magnetic WPs
$\bar{3}m, \bar{3}$	$p\bar{3}'1m'$	2e (3..), 4h (3..)
	$p\bar{3}'1m$	4h (3..)
	$p\bar{3}'m'1$	2c (3m..), 2d (3m..)
	$p\bar{3}'$	2c (3..), 2d (3..)
$4/mmm$	$p4/m'm'm'm'$, $2g(4m'm'm')$, $2h(4m'm'm')$, $4i(2m'm'm')$	
	$p4'/m'm'm'$	$4i(2m'm')$
	$p4/n'b'm'$	4g (4..), 4h (2..)
	$p4/n'bm'$	4g (4..)
	$p4'/n'bm'$	$4h(2..)$
	$p4/m'b'm'$	4e (4..), 4f (2..)
	$p4/m'bm'$	4e (4..)
	$p4/m'n'm'$	4f (2..)
	$p4'/n'm'm'$	$2c(4mm)$, $4f(2m'm')$
	$p4'/n'm'm'$	$4f(2..)$
$4/m$	$p4/m'$	$2g(4..)$, $2h(4..)$, $4i(2..)$
	$p4'/m'$	$4i(2..)$
	$p4/n'$	$2c(4..)$, $4f(2..)$
	$p4'/n'$	$4f(2..)$
$6/mmm$	$p6/m'm'm'$	$2e(6m'm')$, $4h(3m')$, $6i(2m'm')$
	$p6'/mmm'$	$6j(m2'm')$, $12p(m..)$
	$p6'/mm'm$	$4h(3m')$, $6l(mm'2')$, $12p(m..)$
$6/m$	$p6/m'$	$2e(6..)$, $4h(3..)$, $6i(2..)$
	$p6'/m$	$4h(3..)$, $6j(m..)$

layer groups and combining density functional theory (DFT) calculations, we present the band splitting of material candidates, with strength exceeding 20 meV. Be-

yond electric switchability, the weak SOC also ensures the stability of the band splitting and the corresponding spin current at a finite temperature.

Coupling between spin and hidden dipole. We consider a \mathcal{PT} -symmetric antiferromagnet with magnetic layer group G . The G can be decomposed into cosets as $G = H + \mathcal{PT}H + \dots + R_nH$. As \mathcal{PT} is the coset representative, the subgroup H breaks \mathcal{P} symmetry and can therefore be polar, allowing for spontaneous polarization. The H describes the site symmetry of a magnetic Wyckoff position (WP), which ensures that the magnetic atoms are electrically polarized [46, 47]. By screening all \mathcal{PT} -symmetric groups, we identify all polarized magnetic WPs, see results in Tab. 1 and Sec. IV of Supplemental Materials (SM) [45]. Particularly, as shown in Fig. 1(b), we introduce a hidden dipole vector $\lambda(\mathbf{r}_1 - \mathbf{r}_2)$ (\mathbf{r}_1 and \mathbf{r}_2 are position vectors of two magnetic atoms) to capture the compensated polarization. The λ is polar under \mathcal{P} symmetry: $\lambda(\mathbf{r}_1 - \mathbf{r}_2) \rightarrow -\lambda(\mathbf{r}_1 - \mathbf{r}_2)$ and its magnitude is proportional to the distance between two magnetic atoms. The λ implies a giant effective magnetoelectric (ME) coupling coefficient $\chi \propto \lambda M$ (M is local magnetic moment), which is allowed under \mathcal{PT} symmetry and yields a giant Zeeman-like field under external field \mathbf{E} , $B_\alpha = \chi_{\alpha\beta} E_\beta$. Moreover, when the local dipole is coupled with the spin lattice, the polar distortion modifies the electronic wavefunctions and ligand fields in the material, generating an internal effective magnetic field [48–50]. Please note that λ is approximately zero in conventional \mathcal{PT} antiferromagnets [51, 52], and only an external magnetic field can induce a weak band splitting, as shown

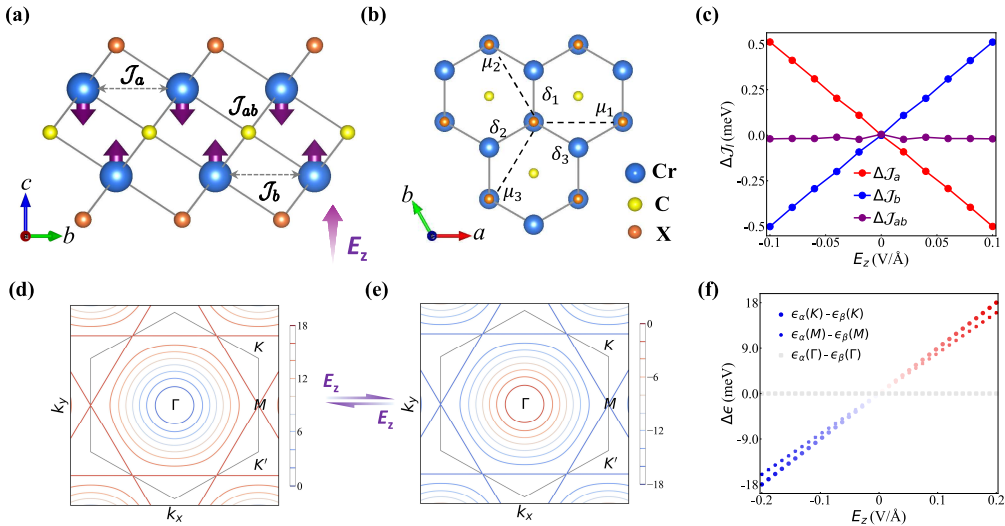


FIG. 2. (a)-(b) The side and top view of the monolayer Cr_2CX_2 where $X = \text{F}, \text{Cl}, \text{Br}$. (c) The changes in the NN spin exchange \mathcal{J}_a , \mathcal{J}_b and \mathcal{J}_{ab} on E_z . Here, only the relative energy differences between the cases with and without the E_z are presented, denoted as $\Delta\mathcal{J}_a$, $\Delta\mathcal{J}_b$ and $\Delta\mathcal{J}_{ab}$, respectively. The relative band splitting energies with (d), $E_z > 0$ and (e) $E_z < 0$. (f) The changes in the splitting strength at high symmetry points on E_z .

in Fig. 1(a).

Next, based on DFT calculations [53–55], we show the magnon band splitting in monolayer Cr_2CF_2 under the electric field. Monolayer Cr_2CF_2 adopts the $p\bar{3}m1$ magnetic layer group, where Cr ions occupy WP 2d (0.333, 0.333, 0.437) with polar site group $3m'$. In Cr_2CF_2 , Cr^{3+} ions adopts $S = 3/2$ insulator states, forming the triangular magnetic lattice in each layer. Obviously, as shown in Fig. 2(b), two Cr layers with opposite layer polarization are stacked in an AB configuration, forming a honeycomb magnetic lattice. DFT calculations show that nearest-neighbor (NN) interlayer spin exchange (\mathcal{J}_{ab}) is antiferromagnetic (AFM) coupling with a strength of 8.3 meV, and the intralayer spin exchanges (\mathcal{J}_a or \mathcal{J}_b) exhibits ferromagnetic coupling with a strength of 9.5 meV, allowing the Néel temperature to exceed room temperature. The local magnetic moments with opposite spin is equal (M_a and M_b) in the absence of the E_z , leading to that $\mathcal{J}_a = \mathcal{J}_b$.

Upon applying E_z , the strong ME coupling distribute the balance between the layers, such as the localized Cr^{3+} spin moments. DFT calculations show that changes of the local magnetic moments reach $0.009 \mu_B$ with E_z of $0.2 \text{ V}/\text{\AA}$, and the ME coupling coefficient χ is determined by $1.1 \times 10^{-7} \text{ s}/\text{m}$. Consequently, it significantly changes the intralayer spin exchanges, as illustrated in Fig. 2(c), where $\mathcal{J}_a - \mathcal{J}_b = -1 \text{ meV}$ for $E_z = 0.1 \text{ V}/\text{\AA}$. As the strength of E_z increases, $\mathcal{J}_a - \mathcal{J}_b$ exhibits a linear dependence on E_z , described by $\mathcal{J}_a - \mathcal{J}_b = -10 E_z$, indicating that electric field can reverse the sign of $\mathcal{J}_a - \mathcal{J}_b$. In contrast, the changes in intralayer spin exchange \mathcal{J}_{ab} and single-ion anisotropy (SIA) is negligible. As shown in Fig. 2(d), the values of \mathcal{J}_{ab} remain approximately equal

in the presence and absence of the electric field, indicating the Néel order remains unchanged under the electric fields.

Chiral split magnons. Building on the above DFT calculations and model analysis, we can construct the effective spin Hamiltonian of monolayer Cr_2CF_2 , expressed as

$$\hat{\mathcal{H}}_s = \mathcal{J}_{ab} \sum_{\langle i,j \rangle} \mathcal{S}_i \cdot \mathcal{S}_j + \sum_{\langle i,j \rangle} \mathcal{J}_a (\mathcal{S}_i \cdot \mathcal{S}_j) + \sum_{\langle i,j \rangle} \mathcal{J}_b (\mathcal{S}_i \cdot \mathcal{S}_j) + \sum_i \mathcal{K} (\mathcal{S}_i^z)^2, \quad (1)$$

where the first term is NN interlayer spin exchanges and the second to third terms refer to the NN intralayer spin exchanges. The linear spin wave model in Eq. (1) can be solved by employing Holstein-Primakoff (HP) transformation [56], $\mathcal{S}_{i,\uparrow}^+ \approx \sqrt{2S} \hat{a}_i$, $\mathcal{S}_{i,\downarrow}^- \approx \sqrt{2S} \hat{b}_i$, $\mathcal{S}_{i,\uparrow}^z = S - \hat{a}_i^\dagger \hat{a}_i$ and $\mathcal{S}_{i,\downarrow}^z = \hat{b}_i^\dagger \hat{b}_i - S$, where $\hat{a}_i^\dagger (\hat{b}_i^\dagger)$ creates a magnon on sublattice in the i -th unit cell. Upon Fourier transformation, the Hamiltonian can be expressed in the spinor basis $\psi_{\mathbf{k}}^\dagger \equiv (\hat{a}_{\mathbf{k}}, \hat{b}_{-\mathbf{k}})$ as $\hat{\mathcal{H}} = \sum_{\mathbf{k}} \psi_{\mathbf{k}}^\dagger \hat{\mathcal{H}}_{\mathbf{k}} \psi_{\mathbf{k}}$. $\hat{\mathcal{H}}_{\mathbf{k}}$ reads as,

$$\frac{\hat{\mathcal{H}}_{\mathbf{k}}}{S} = 3\mathcal{J}_{ab} - 2\mathcal{K} + f_{\mathbf{k}}^+ + \begin{pmatrix} +f_{\mathbf{k}}^- & \gamma_{\mathbf{k}} \\ \gamma_{\mathbf{k}}^\dagger & -f_{\mathbf{k}}^- \end{pmatrix}, \quad (2)$$

where

$$\gamma_{\mathbf{k}} = \mathcal{J}_{ab} \sum_{\mathbf{k}, \delta_i} e^{i\mathbf{k} \cdot \delta_i}, \quad (3)$$

$$f_{\mathbf{k}}^\pm = \frac{1}{2} (\mathcal{J}_a \pm \mathcal{J}_b) \sum_{\mathbf{k}, \mu_i} 2\cos(\mathbf{k} \cdot \mu_i) - 6,$$

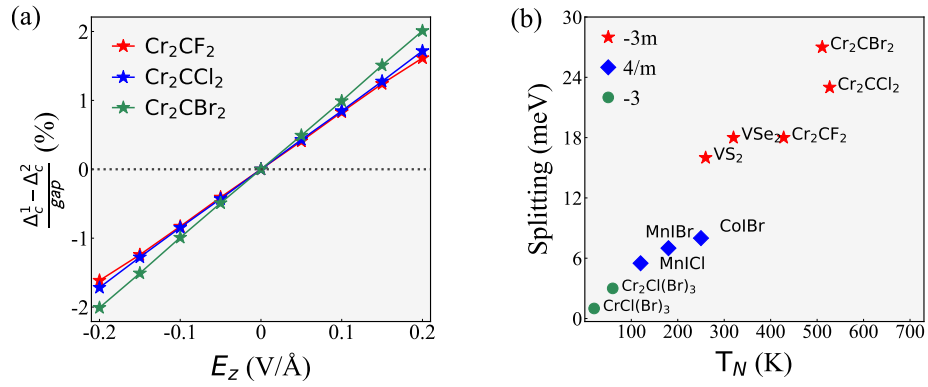


FIG. 3. (a) DFT calculated E_z dependence of normalized $\frac{\Delta_c^1 - \Delta_c^2}{gap}$ of for Cr_2CX_2 . Here, Δ_c^1 and Δ_c^2 refer to the crystal field splitting within the first layer and second layer of Cr^{3+} ions, respectively, and gap refers to the band gap of the material. (b) The band splitting varies material candidates with $E_z = 0.2 \text{ V/Å}$. The T_N of candidates is also listed.

with δ_i and μ_i being the NN and 2NN linking vectors between Cr^{3+} ions as shown in Fig. 2(b).

The Eq. (2) can be diagonalized by the Bogoliubov transformation [51, 52, 57, 58], where the two physical solutions are given by

$$\epsilon_{\mathbf{k}}^{\pm}/S = \sqrt{[f_{\mathbf{k}}^+ + 3\mathcal{J}_{ab} - 2\mathcal{K}]^2 - |\gamma_{\mathbf{k}}|^2} \pm f_{\mathbf{k}}^- . \quad (4)$$

Clearly, two magnon modes, denoted as α and β , are degenerate in the entire Brillouin zone when $E_z = 0$, corresponding to $\mathcal{J}_a = \mathcal{J}_b$. Since the Eq. (2) is block diagonal, spin angular momentum along the z -direction, $\langle s_z \rangle$, is conserved. As a result, α and β magnon modes carry opposite $\langle s_z \rangle$, with chirality ∓ 1 , respectively.

The nonzero $\mathcal{J}_a - \mathcal{J}_b$ naturally breaks the degeneracy between α and β modes. For $E_z > 0$, the strength of \mathcal{J}_a is larger than \mathcal{J}_b , lifts the α mode is high in energy than β mode expect for Γ point. This ordering is inverted when $E_z < 0$. Compared with the magnon band splitting induced by an external magnetic field, the electric-field-induced band splitting exhibits anisotropy. Apart from the degeneracy at Γ point, the magnitude of the splitting varies along the K-M path. As shown in Figs. 2(d)-(f), the largest gap locate at the K-points, given as

$$\Delta_{\epsilon}(\text{K}) = 9 |\mathcal{J}_a - \mathcal{J}_b| . \quad (5)$$

Given that $\mathcal{J}_a - \mathcal{J}_b = -10 E_z$, $\Delta_{\epsilon}(\text{K})$ reaches at 18 meV when $E_z = 0.2 \text{ V/Å}$ for Cr_2CF_2 . The strength of the magnetic field required to induce the same order magnon band splitting can be approximately expressed as

$$B_e = \frac{\Delta_{\epsilon}(\text{K})}{g_s s_z} , \quad (6)$$

where $s_z = 1$ and g_s is the effective g factor with assuming to 1. From Eq. (5) and Eq. (6), the E_z produces a B_e field as large as 155 T. The thermal stability of magnon band splitting is confirmed by the renormalized

spin wave theory (RSWT), with details shown in Section. III of SM [45, 59]. Unlike spin splitting induced by SOC, which leads to band instability due to spin relaxation and dissipation effects, the magnon band splitting induced by the electric field in Cr_2CF_2 with weaker SOC remains stable even above room temperature.

Additionally, we present the magnon band splitting of Cr_2CCl_2 and Cr_2CBr_2 under the electric field. The calculated $\mathcal{J}_a - \mathcal{J}_b$ for Cr_2CCl_2 and Cr_2CBr_2 at $E_z = 0.2 \text{ V/Å}$ are 1.3 meV and 1.55 meV, respectively, corresponding to $\Delta_{\epsilon}(\text{K})$ of 23 meV and 27 meV. These values are significantly larger than those observed in Cr_2CF_2 . Notably, the χ of Cr_2CCl_2 and Cr_2CBr_2 are about $1.0 \times 10^{-7} \text{ s/m}$, even smaller than that of Cr_2CF_2 , hence, the observed difference may arise from the further modulation of the superexchange mechanism between adjacent layers by E_z . To clarify this, we analyze the parameter dependence of superexchange interactions using a multi-orbital model, given as:

$$\begin{aligned} \mathcal{H}_e = & \sum_{\mu, v} \sum_{\sigma} (t_{i\mu jv, \sigma} c_{i\mu, \sigma}^{\dagger} c_{jv, \sigma} + h.c.) \\ & + \sum_{l, \mu} \epsilon_{l\mu} c_{l\mu\sigma}^{\dagger} c_{l\mu\sigma} - \sum_{l, \mu} \frac{U_l}{2} \mathbf{m}_l \cdot \mathcal{S}_{l\mu} . \end{aligned} \quad (7)$$

Here, $l = i, j$ represent the two magnetic sites, μ is the orbital index, ϵ_{μ} denotes the on-site energy of μ -orbital, U represents the exchange split, \mathcal{S} is the spin operator, and \mathbf{m} is the unit vector specifying the magnetization direction. As a result, the crystal splitting Δ_c is defined as $\epsilon_{l2} - \epsilon_{l1}$. Applying the second-order perturbation theory [60], we deduce the form of the spin exchanges, as $-2t^2 \left(\frac{1}{\Delta_c} + \frac{1}{U + \Delta_c} + \frac{1}{U} \right)$. Given that U is robust under the applied electric field, $\mathcal{J} \propto 1/\Delta_c$. As a result, in the absence of E_z , the Δ_c of Cr^{3+} ions in both layers is identical, enforcing $\mathcal{J}_a = \mathcal{J}_b$. However, when $E_z < 0$, the first layer exhibits a larger Δ_c than the second layer, leading to $|\mathcal{J}_a| < |\mathcal{J}_b|$. Conversely, a positive E_z reverses this

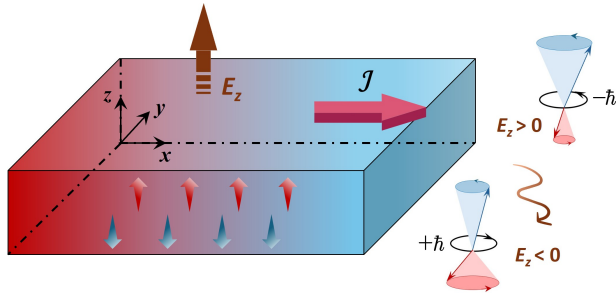


FIG. 4. Illustration of electric switchable spin currents mediated by the magnons in antiferromagnetic insulators. Here, the transition from red to blue represents the distribution of the applied temperature gradient.

trend, hence $|\mathcal{J}_a| > |\mathcal{J}_b|$.

Fig. 3(a) shows the E_z dependence of normalized $\frac{\Delta_c^1 - \Delta_c^2}{\text{gap}}$ for Cr_2CX_2 , where Δ_c^1 and Δ_c^2 refer to the crystal field splitting within first layer and second layer of Cr^{3+} ions, respectively, and gap refer to the band gap of the material. The layer-resolved difference in Δ_c and band gap both determine the electric-field sensitivity of $\mathcal{J}_a - \mathcal{J}_b$. Clearly, the Cr_2CBr_2 responds much more strongly than the Cr_2CCl_2 and Cr_2CF_2 , explaining the distinct electric-field dependence of their intralayer spin exchange. Guided by symmetry analysis and high-throughput calculations, we systematically examine magnon band splitting in antiferromagnets with hexagonal and tetragonal crystal symmetries. As shown in Fig. 3(b), the candidates with higher T_N and narrow band gap generally exhibit larger magnon band splittings.

Electric-switchable Spin currents. The giant chiral splitting of magnons naturally leads to a spin current driven by the applied temperature gradient ∇T (see Fig. 4), known as the spin Seebeck effect [3, 13, 14, 39, 61]. The thermal spin conductivity tensor σ_{mn} is defined by $\langle \mathbf{j} \rangle_m = -\sigma_{mn}(\nabla T)_n$, where $m, n \in \{x, y\}$, $\langle \mathbf{j} \rangle$ is the spin current density. Based on the Kubo formula [45], the spin conductivity σ_{mn} is given as

$$\sigma_{xy} = \sum_{s=\mp} \sum_{\mathbf{k}, \lambda=\pm} \frac{s\tau_0}{\hbar k_B V T^2} \mathbf{v}_{x,\mathbf{k}}^\lambda \mathbf{v}_{y,\mathbf{k}}^\lambda \frac{e^{\epsilon_{\mathbf{k}}^\lambda/k_B T}}{\left(e^{\epsilon_{\mathbf{k}}^\lambda/k_B T} - 1\right)^2} \quad (8)$$

where $\mathbf{v}_{\mathbf{k}}^\lambda = \partial \epsilon_{\mathbf{k}}^\lambda / \hbar \partial \mathbf{k}$, V is the volume, τ_0 is the average magnon lifetime. The thermal spin conductivity tensor is anisotropic and could be simplified into a scalar $\sigma = \sigma_{xx} = \sigma_{yy}$ as $\sigma_{xy} = \sigma_{yx} = 0$.

The linear dependence of thermal spin conductivity on applied electric field is shown in Fig. S4 [45]. For $E_z = 0.1 \text{ V}/\text{\AA}$, $\sigma = 0.102 \text{ meV}/\text{K}$ at $T = 300 \text{ K}$, which is three orders in magnitude larger than that induced by nonzero spin Berry curvature in monolayer and bilayer antiferromagnets. As for $E_z < 0$, the bandwidth

$\epsilon_\beta(\text{K}) - \epsilon_\beta(\Gamma)$ exceeds $\epsilon_\alpha(\text{K}) - \epsilon_\alpha(\Gamma)$, and consequently the effective velocity $\mathbf{v}_\mathbf{k}^\alpha$ exceeds $\mathbf{v}_\mathbf{k}^\beta$. As a result, the contribution to the spin conductivity from the β band is larger than that from the α band, leading to a positive spin conductivity. Since the α and β magnon modes carry opposite $\langle s_z \rangle$, the electric field switches the sign of the spin current while also altering the intrinsic spin angular momentum information encoded, as shown in Fig. 4. This opens up new avenues for the electric-field-controlled spintronics based on the magnons.

Summary and discussion. The magnon band splitting induced by the electric field breaks the antiferromagnetic lattice symmetry but is independent of the SOC effect. As a result, the split magnon bands still conserve spin angular momentum. This behavior is distinct from the splitting caused by SOC, which can lead to magnon dissipation, and thus the electric field-induced splitting demonstrates greater stability. Furthermore, it is important to note that all the candidate systems we have listed are insulators, which effectively prevents the band damping [1, 2, 38, 62].

In summary, we have identified a class of \mathcal{PT} -preserving AFIs featuring in giant magnon bands splitting by the electric field. By first-principles calculations and linear spin wave calculations, we demonstrate that the magnon band splitting of various candidates reach up to 20 meV under an electric field of $0.2 \text{ V}/\text{\AA}$. These candidates exhibit large band splittings, exceptional stability, and the ability to propagate in insulating systems, positioning our approach as a promising route for nonvolatile magnon-based devices.

Acknowledgments. This work is supported by the National Natural Science Foundation of China (Grant No. 12374092), Natural Science Basic Research Program of Shaanxi (Program No. 2023-JC-YB-017), Shaanxi Fundamental Science Research Project for Mathematics and Physics (Grant No. 22JSQ013), “Young Talent Support Plan” of Xi'an Jiaotong University, and the Xiaomi Young Talents Program. G. Q. Chang thanks grants from the Singapore National Research Foundation Fellowship Award (NRF-NRFF13-2021-0010) and Nanyang Technological University startup grant (NTUSUG). Y. Jin thanks to the Guangdong Provincial Quantum Science Strategic Initiative (Grant No. GDZX2401002), the Natural Science Foundation of China (Grant No. 12404181).

Data availability. All data are available from the authors upon reasonable request.

* These authors contributed equally to this work

† zjjiang@xjtu.edu.cn

‡ yuanjunjin@m.scnu.edu.cn

§ guoqing.chang@ntu.edu.sg

[1] A. V. Chumak, A. A. Serga, and B. Hillebrands, *Nat. Commun.* **5**, 4700 (2014).

[2] A. V. Chumak, V. I. Vasyuchka, A. A. Serga, and B. Hillebrands, *Nat. Phys.* **11**, 453 (2015).

[3] Y. Onose, T. Ideue, H. Katsura, Y. Shiomi, N. Nagaosa, and Y. Tokura, *Science* **329**, 297 (2010).

[4] S. D. Bader and S. S. P. Parkin, *Annu. Rev. Condens. Matter Phys.* **1**, 71 (2010).

[5] P. Pirro, V. I. Vasyuchka, A. A. Serga, and B. Hillebrands, *Nat. Rev. Mater.* **6**, 1114 (2021).

[6] P. A. McClarty, *Annu. Rev. Condens. Matter Phys.* **13**, 171 (2022).

[7] B. Lenk, H. Ulrichs, F. Garbs, and M. Münzenberg, *Phys. Rep.* **507**, 107 (2011).

[8] X. Chen, Y. Liu, P. Liu, Y. Yu, J. Ren, J. Li, A. Zhang, and Q. Liu, *Nature* **640**, 349 (2025).

[9] L. Chen, J.-H. Chung, B. Gao, T. Chen, M. B. Stone, A. I. Kolesnikov, Q. Huang, and P. Dai, *Phys. Rev. X* **8**, 041028 (2018).

[10] A. Mook, K. Plekhanov, J. Klinovaja, and D. Loss, *Phys. Rev. X* **11**, 021061 (2021).

[11] Y. Onose, T. Ideue, H. Katsura, Y. Shiomi, N. Nagaosa, and Y. Tokura, *Science* **329**, 297 (2010).

[12] X.-T. Zhang, Y. H. Gao, and G. Chen, *Phys. Rep.* **1070**, 1 (2024).

[13] R. Cheng, S. Okamoto, and D. Xiao, *Phys. Rev. Lett.* **117**, 217202 (2016).

[14] V. A. Zyuzin and A. A. Kovalev, *Phys. Rev. Lett.* **117**, 217203 (2016).

[15] S. Qi, D. Chen, K. Chen, J. Liu, G. Chen, B. Luo, H. Cui, L. Jia, J. Li, M. Huang, *et al.*, *Nat. Commun.* **14**, 2526 (2023).

[16] C. Liu, Y. Luo, D. Hong, S. S.-L. Zhang, H. Saglam, Y. Li, Y. Lin, B. Fisher, J. E. Pearson, J. S. Jiang, and et al., *Sci. Adv.* **7**, 1669 (2021).

[17] A. M. Kuzmenko, D. Szaller, T. Kain, V. Dziom, L. Weymann, A. Shubaev, A. Pimenov, A. A. Mukhin, V. Y. Ivanov, I. A. Gudim, L. N. Bezmaternykh, and A. Pimenov, *Phys. Rev. Lett.* **120**, 027203 (2018).

[18] X. Wan, Q. Du, J. Lu, Z. Zhang, J. Ni, L. Zhang, Z. Jiang, and L. Bellaiche, *Phys. Rev. B* **112**, L100404 (2025).

[19] A. Rückriegel, A. Brataas, and R. A. Duine, *Phys. Rev. B* **97**, 081106 (2018).

[20] E. Parsonnet, L. Caretta, V. Nagarajan, H. Zhang, H. Taghinejad, P. Behera, X. Huang, P. Kavle, A. Fernandez, D. Nikonorov, and et al., *Phys. Rev. Lett.* **129**, 087601 (2022).

[21] Y.-P. Wang, J. W. Rao, Y. Yang, P.-C. Xu, Y. S. Gui, B. M. Yao, J. Q. You, and C.-M. Hu, *Phys. Rev. Lett.* **123**, 127202 (2019).

[22] V. Baltz, A. Manchon, M. Tsui, T. Moriyama, T. Ono, and Y. Tserkovnyak, *Rev. Mod. Phys.* **90**, 015005 (2018).

[23] T. Jungwirth, X. Marti, P. Wadley, and J. Wunderlich, *Nat. Nanotechnol.* **11**, 231 (2016).

[24] S. M. Rezende, A. Azevedo, and R. L. Rodríguez-Suárez, *J. Appl. Phys.* **126** (2019).

[25] O. Gomonay, V. Baltz, A. Brataas, and Y. Tserkovnyak, *Nat. Phys.* **14**, 213 (2018).

[26] R. R. Neumann, A. Mook, J. Henk, and I. Mertig, *Phys. Rev. Lett.* **128**, 117201 (2022).

[27] G. Gitgeatpong, Y. Zhao, P. Piyawongwatthana, Y. Qiu, L. W. Harriger, N. P. Butch, T. Sato, and K. Matan, *Phys. Rev. Lett.* **119**, 047201 (2017).

[28] T. J. Sato and K. Matan, *J. Phys. Soc. Jpn.* **88**, 081007 (2019).

[29] T. Matsumoto and S. Hayami, *Phys. Rev. B* **101**, 224419 (2020).

[30] S. Hayami and T. Matsumoto, *Phys. Rev. B* **105**, 014404 (2022).

[31] L. Šmejkal, J. Sinova, and T. Jungwirth, *Phys. Rev. X* **12**, 031042 (2022).

[32] L. Šmejkal, J. Sinova, and T. Jungwirth, *Phys. Rev. X* **12**, 040501 (2022).

[33] S. Hayami, Y. Yanagi, and H. Kusunose, *J. Phys. Soc. Jpn.* **88**, 123702 (2019).

[34] Z. Xiao, J. Zhao, Y. Li, R. Shindou, and Z.-D. Song, *Phys. Rev. X* **14**, 031037 (2024).

[35] X. Chen, J. Ren, Y. Zhu, Y. Yu, A. Zhang, P. Liu, J. Li, Y. Liu, C. Li, and Q. Liu, *Phys. Rev. X* **14**, 031038 (2024).

[36] Y. Jiang, Z. Song, T. Zhu, Z. Fang, H. Weng, Z.-X. Liu, J. Yang, and C. Fang, *Phys. Rev. X* **14**, 031039 (2024).

[37] P. Liu, J. Li, J. Han, X. Wan, and Q. Liu, *Phys. Rev. X* **12**, 021016 (2022).

[38] L. Šmejkal, A. Marmodoro, K.-H. Ahn, R. González-Hernández, I. Turek, S. Mankovsky, H. Ebert, S. W. D’Souza, O. Šipr, J. Sinova, *et al.*, *Phys. Rev. Lett.* **131**, 256703 (2023).

[39] K. Wu, J. Dong, M. Zhu, F. Zheng, and J. Zhang, *Chin. Phys. Lett.* (2025).

[40] Z. Liu, M. Ozeki, S. Asai, S. Itoh, and T. Masuda, *Phys. Rev. Lett.* **133**, 156702 (2024).

[41] V. C. Morano, Z. Maesen, S. E. Nikitin, J. Lass, D. G. Mazzone, and O. Zaharko, *Phys. Rev. Lett.* **134**, 226702 (2025).

[42] Y.-F. Zhang, X.-S. Ni, K. Chen, and K. Cao, *Phys. Rev. B* **111**, 174451 (2025).

[43] M. Alaei, P. Sobieszczyk, A. Ptak, N. Rezaei, A. R. Oganov, and A. Qaiumzadeh, *Phys. Rev. B* **111**, 104416 (2025).

[44] Q. Sun, J. Guo, D. Wang, D. L. Abernathy, W. Tian, and C. Li, *Phys. Rev. Lett.* **135**, 186703 (2025).

[45] Supporting Information includes I. Additional details of DFT calculations; II. magnon transport theory; III. the finite temperature behavior of magnons; and IV. the symmetry analysis.

[46] M. Fiebig, *J. Phys. D* **38**, R123 (2005).

[47] J. Ni, Z. Zhang, J. Lu, Q. Du, Z. Jiang, and L. Bellaiche, *Nano Lett.* **25**, 1207 (2025).

[48] H. J. Zhao, X. Liu, Y. Wang, Y. Yang, L. Bellaiche, and Y. Ma, *Phys. Rev. Lett.* **129**, 187602 (2022).

[49] L. Tao, Q. Zhang, H. Li, H. J. Zhao, X. Wang, B. Song, E. Y. Tsymbal, and L. Bellaiche, *Phys. Rev. Lett.* **133**, 096803 (2024).

[50] L. Yu, H. J. Zhao, L. Bellaiche, and Y. Ma, *Phys. Rev. Lett.* **135**, 256704 (2025).

[51] J. Ni, Y. Jin, Q. Du, and G. Chang, *Phys. Rev. B* **112**, 054424 (2025).

[52] Q. Du, Z. Zhang, J. Ni, Z. Jiang, and L. Bellaiche, *Phys. Rev. B* **112**, L100408 (2025).

[53] H. Xiang, E. Kan, S.-H. Wei, M.-H. Whangbo, and X. Gong, *Phys. Rev. B* **84**, 224429 (2011).

[54] H. Xiang, C. Lee, H.-J. Koo, X. Gong, and M.-H. Whangbo, *Dalton Trans.* **42**, 823 (2013).

[55] J. Ni, X. Li, D. Amoroso, X. He, J. Feng, E. Kan, S. Piccozzi, and H. Xiang, *Phys. Rev. Lett.* **127**, 247204 (2021).

[56] T. Holstein and H. Primakoff, *Phys. Rev.* **58**, 1098 (1940).

[57] N. N. Bogoljubov, V. V. Tolmachev, and D. Širkov,

Fortschr. Phys. **6**, 605 (1958).

[58] J. Valatin, Il Nuovo Cimento (1955-1965) **7**, 843 (1958).

[59] K. Sourounis and A. Manchon, Phys. Rev. B **110**, 054429 (2024).

[60] R. Winkler, *Spin-Orbit Coupling Effects in Two-Dimensional Electron and Hole Systems*, Springer Tracts in Modern Physics (Springer, Berlin, Heidelberg, 2003).

[61] Q. Cui, B. Zeng, P. Cui, T. Yu, and H. Yang, Phys. Rev. B **108**, L180401 (2023).

[62] G. Poelchen, J. Hellwig, M. Peters, D. Y. Usachov, K. Kliemt, C. Laubschat, P. M. Echenique, E. V. Chulkov, C. Krellner, S. Parkin, *et al.*, Nat. Commun. **14**, 5422 (2023).